Science of the Total Environment 954 (2024) 176284

Contents lists available at ScienceDirect

Science of the Total Environment

journal homepage: www.elsevier.com/locate/scitotenv

Oxidative weathering of pyrite in acidic environments: Data-driven experimental evaluation coupled with Raman hyperspectral imaging

Enmanuel Cruz Muñoz [a], Fabio Gosetti [a,*], Sergio Andò [b], Davide Ballabio [a], Eduardo Garzanti [b]

[a] Milano Chemometrics and QSAR Research Group, Department of Earth and Environmental Sciences - DISAT, University of Milano-Bicocca, Milan, Italy
[b] Laboratory for Provenance Studies, Department of Earth and Environmental Sciences - DISAT, University of Milano-Bicocca, Milan, Italy

HIGHLIGHTS

- Elemental sulfur is a noticeable weathering product of pyrite in acidic environments.
- Ferric iron, crystal size and humic acids presence were identified as relevant factors.
- Mass loss is correlated with elemental sulfur production.
- Elemental sulfur is homogeneously distributed in patches of at least 600 μm^2.

GRAPHICAL ABSTRACT

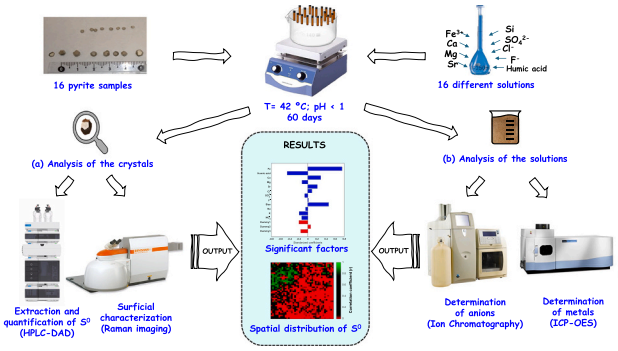

ARTICLE INFO

Editor: Daniel Alessi

Keywords:
Oxidative weathering of pyrite
Ferric iron
Elemental sulfur
Plackett-Burman design
Raman spectroscopy
Hyperspectral image analysis

ABSTRACT

This study deals with the identification of the factors that affect pyrite oxidation in acid mine drainage conditions. For this scope, weathering experiments have been carried at laboratory scale based on the design of experiments methodology to evaluate the effect of factors such as major ion concentrations, crystal size, and humic acids presence over the amount of elemental sulfur produced due to the involved weathering reactions. In particular, metal and anionic concentrations in solution were quantified by inductively coupled plasma-atomic emission spectroscopy and ion-chromatography techniques, respectively, whereas the amount of elemental sulfur was quantified with a high-performance liquid chromatography with diode-array detection technique after proper extraction procedure. A partial least squares regression was calculated to establish a quantitative relationship between the considered factors and the amount of elemental sulfur. After evaluation of the model, ferric iron, crystal size and the presence of humic acids were identified as the relevant factors for pyrite oxidation under acidic conditions. In addition, the surface of the samples was characterized by Raman imaging spectroscopy and subsequently analyzed by explorative hyperspectral analysis methods to assess the spatial distribution of the elemental sulfur as the main weathering product, resulting in a homogenous distribution.

* Corresponding author.
E-mail address: fabio.gosetti@unimib.it (F. Gosetti).

https://doi.org/10.1016/j.scitotenv.2024.176284
Received 3 May 2024; Received in revised form 18 August 2024; Accepted 12 September 2024
Available online 13 September 2024

1. Introduction

Pyrite (FeS_2) is the most abundant sulfide on the Earth's surface, constituting over 95 % of total sulfides (Vaughan and Corkhill, 2017). It is found mainly in sedimentary rocks (e.g., organic-rich black mudrocks), but also in ores (e.g., porphyry copper deposits), intrusive mafic and ultramafic rocks (e.g., in association with ophiolite complexes), as large masses in skarn deposits formed by contact metamorphism, or in hydrothermal veins. The main source of biogenic pyrite is represented by sulfate-reducing microorganisms, which are ubiquitous on the planet and provide a set of enzymes to promote the oxidation of organic matter and the reduction of S^{6+} in sulfates to S^{2-} in the form of hydrogen sulfide via an 8-electron mechanism, which reacts with dissolved Fe^{2+} to produce pyrite and other metastable iron sulfides (Rickard et al., 2017; Zhang et al., 2022). Although pyrite is widely used in the production of sulfuric acid (Jameson, 2011), its economic value is lower compared to other commonly associated minerals such as chalcopyrite, galena, and sphalerite, although pyrite may locally carry gold dispersions (Wenk and Bulakh, 2004). Pyrite is a key mineral to understand Earth's climate change at geological scale, because it is involved in the global carbon, oxygen, and sulfur cycles (Berner, 1987, 2009; Calmels et al., 2007; Torres et al., 2014; Bufe et al., 2021).

The reverse reaction of pyrite formation, which is called oxidative weathering of pyrite (OWP), is the main responsible for the acidification of natural waters, also known as acid mine drainage (AMD) if caused by anthropogenic action. Atmospheric oxidation may generate products such as sulfates, polysulfides (S_n^{2-}), or iron oxy-hydroxide (FeOOH) species (Buckley and Woods, 1987; de Donato et al., 1993; Schaufuß et al., 1998; Todd et al., 2003). Aqueous oxidation, which is faster than atmospheric oxidation, mainly releases sulfate and ferric iron into solution. Depending on environmental conditions (e.g., calcareous or acidic media) oxidation products also include polysulfides, elemental sulfur (S^0), ferric hydroxide precipitates, iron oxides (mainly Fe_3O_4 or Fe_2O_3), oxy-hydroxide species, hydrogen sulfide, sulfite (SO_3^{2-}), polythionates ($S_XO_6^{2-}$), and thiosulfates ($S_2O_3^{2-}$) intermediates (McKibben and Barnes, 1986a; Moses et al., 1987; Sasaki et al., 1997; Giannetti et al., 2001; Demoisson et al., 2007; Chandra and Gerson, 2010; Muñoz et al., 2023). Although OWP is a complex mechanism that takes place via several chemical reactions, the main ones can be summarized as follows:

$$2FeS_2 + 7O_2 + 2H_2O \rightarrow 2Fe^{2+} + 4SO_4^{2-} + 4H^+ \quad (1)$$

$$4Fe^{2+} + O_2 + 4H^+ \rightarrow 4Fe^{3+} + 2H_2O \quad (2)$$

$$FeS_2 + 14Fe^{3+} + 8H_2O \rightarrow 15Fe^{2+} + 2SO_4^{2-} + 16H^+ \quad (3)$$

If oxygen is the only oxidant present in water molecules (1), then oxidation releases sulfate and ferrous iron into solution, which further oxides into ferric iron (2). However, when soluble ferric iron is present in high concentration, it replaces oxygen as a more efficient oxidant agent (McKibben and Barnes, 1986b; Moses et al., 1987), also producing sulfate and ferrous iron (3). In addition, acidophilic microorganisms such as *Acidithiobacillus ferrooxidans* also play an important role by accelerating the oxidation of pyrite in acid mine waters. This biologically mediated oxidation could be classified into indirect, direct and synergistic mechanisms (Fowler et al., 2001; Yu et al., 2001; Zhu and Reinfelder, 2012; Yang et al., 2015).

Despite the complexity of the OWP mechanism, the diverse chemical paths, and the numerous intermediate species and weathering products involved, a certain consensus has been reached on the chemical and morphological factors that modulate the weathering of pyrite in different scenarios (Singer and Stumm, 1970; Margitan, 1984; Buckley and Woods, 1987; Moses et al., 1987; Brown and Jurinak, 1989; Moses and Herman, 1991; Evangelou and Zhang, 1995; Kelsall et al., 1999; Holmes and Crundwell, 2000; Keith and Vaughan, 2000). The aim of the present study is the assessment of the effect of several factors on pyrite oxidation in extreme acidic conditions such as AMD environments by simulation experiments of OWP supported by Design of Experiments (DoE) conducted at laboratory scale. The surface characterization of pyrite samples was carried out by Raman spectroscopy and subsequent hyperspectral image analysis was used for the identification of the main weathering products produced under the studied conditions and their spatial distribution. For this purpose, several pyrite crystals were initially treated chemically to obtain fresh samples as starting material and then immersed in different acidic solutions at controlled temperature to promote pyrite oxidation for two months. The characterization of the surface was carried out at the end of the experiments and the deposited sulfur was extracted, quantified, and used as a proxy for the screening of the different factors under investigation.

2. Material and methods

2.1. Mineralogical samples

The analyzed samples are 19 dodecahedral crystals of pyrite with diameter ranging from 1 to 3 mm and similar shape. Samples are all from a locality in Val Trebbia (Piacenza province, northern Italy), well described in the literature (Jervis, 1874, G G., 2008), where marcasite, pyrite and radiating baryte are commonly found in marls and red clays belonging to the Cretaceous Liguride units (Argille Scagliose).

2.2. Reagents

Ethanol (ACS grade), hydrochloric acid (fuming 37 %) and methanol (HPLC grade) were purchased from Carlo Erba (Milan, Italy). Perchloroethylene (HPLC grade) was purchased from Honeywell (Milan, Italy). Sodium, potassium, calcium, magnesium, strontium (ICP-OES standards), as well as nitrogen, sulfate, chloride, fluoride, phosphate (ion chromatography standards), iron nitrate nonahydrate (ACS grade) and carbon disulfide (ACS grade) were purchased from Chem-Lab (Zedelgem, Belgium). Humic acid sodium salt, silicon (ICP-OES standard) and elemental sulfur (99.998 % purity) were purchased from Sigma-Aldrich (Milano, Italy). Ultrapure water was produced by a Millipore Milli-Q system (Milford, USA).

2.3. Instrumentation

Metal elements (Na, K, Ca, Mg, Si, Sr, and total Fe) were determined by using an ICP OES Optima 7000 DV (PerkinElmer, Italy) system. Water soluble inorganic anions (Cl^-, F^-, NO_3^- and SO_4^{2-}) were determined with a Dionex ICS-2000 IC (Thermo Fisher, Italy) system equipped with an Ion Pac AS14A-5 μm column (Thermo Fisher, Italy), with guard column AG14A-5 μm and a CCD array detector. Elemental sulfur was determined a HPLC-DAD Infinity 1260 (Agilent, Italy) system equipped with a Zorbax Eclipse C18 (150 × 4.6 mm, 3.5 μm) column (Agilent, Italy). Raman spectra were collected using an inVia Qontor™ confocal Raman spectrometer (Renishaw, UK), equipped with 1800 lines/mm (vis) grating and edge filter for the excitation beam laser at 532 nm (theoretical laser-spot diameter ~ 0.84 μm) at 5 % power reduced by a neutral filter. The spectrometer was calibrated using the 520.5 cm^{-1} line of a standard monocrystalline silicon wafer. Preliminary tests were carried out to identify the maximum exposure time, laser power and number of accumulations, most appropriate to avoid warming up and altering the chemical surface. Acquisition conditions (slit opening 65 μm, exposure time 0.5 s, three accumulations per spectrum) were thus chosen to avoid unintentional transformations into new mineralogical phases during prolonged exposure to laser radiation.

2.4. Experimental design

DoE methodology was carried out to screen 13 different factors. These factors are controlled properties set to a certain value when

planning an experiment. To quantitively estimate the effect of the evaluated factors on pyrite weathering, it is necessary to measure a property linked to the oxidative mechanism. This property, also known as response, must be a direct consequence of the combination of the factors. Since the experiments were carried out mimicking extreme AMD conditions and because the action of ferric iron as oxidant was expected, elemental sulfur produced via thiosulfate pathway and then deposited on the surface of pyrite was extracted, quantified and considered as the response in DoE.

DoE aims at establishing the relationship between factors x and the response (property) y by means of linear modelling:

$$y = b_0 + \sum_{k=1}^{K} b_k x_k \quad (4)$$

where K is the number of factors, b_k is the k-th coefficient that expresses the effect of the k-th factor and x_k is the value associated to the k-th factor. Therefore, effects of factors associated to coefficients close to zero can be considered not significant for the response, whereas large coefficients highlight those factors that affect the response positively or negatively.

Table S1 collects the list of considered factors and their experimental domains, which were delimited according to major ions real water chemistry data on some world rivers (Madhavan and Subramanian, 2001; Samanta et al., 2019; Tsering et al., 2019; Cartwright, 2020; Kemeny et al., 2021; Amrish et al., 2022). In contrast, experimental domains of humic acid, size and ferric iron concentrations were established based on previous personal experiences carried out in the laboratory for the oxidation of pyrite. Among the considered factors, 3 out of 13 (sodium, potassium, and nitrate concentrations) were considered as uncontrolled because of the noticeable presence of these elements as counterions in some of the reagents employed.

Plackett-Burman designs are considered very efficient for the screening of a large number of factors, as in this case (Torrijos and Phan-Tan-Luu, 2020). Therefore, DoE based on Plackett-Burman was carried out, each factor being analyzed on two levels, which correspond to the maximum and minimum values of the experimental domain. A total of 16 experiments were carried out, each summarized in the experimental plan shown in Table S2, along with the sample labels (from N1 to N16) to be used hereafter.

2.5. Experimental procedure and setup

Pyrite crystals were chemically treated by adapting the protocol described in (McGuire et al., 2001). First, minerals were ultrasonically washed in ethanol for 30 min to remove any added particles or organic matter onto the surface and then treated with a solution of HCl (1.5 M) overnight to remove any previous oxidation layer. Some publications supported this acidic treatment as a good starting point for oxidation experiments because the surface exhibits a similar reactivity to that of cleaved pyrite (Elsetinow et al., 2003). Crystals were then treated for two hours with carbon disulfide to remove any previous elemental sulfur on the surface. To check the surficial composition of the crystals after this chemical treatment, several Raman punctual analyses were carried out on different points of the surface to check whether surficial pyrite was altered or not, resulting in all cases in the three typical vibrational modes of pyrite at ca. 343, 378 and 429 cm^{-1}. One of the sixteen pyrite samples was randomly selected and Raman maps of a recognizable area both before and after the conclusion of the weathering experiments were acquired for comparison. Stock solutions were freshly prepared for each of the chemical factors considered in the DoE.

The experimental setup was as follows: a) pre-treated pyrite crystals were accurately weighed and grouped according to the size factor; b) several solutions equal to the number of experiments were prepared. In each case, the volume of the fresh stock solutions to be added was adjusted to obtain a final concentration for each of the factors equal to the level of that factor on that experiment according to the experimental plan shown in Table S2; c) 10.0 mL of each solution was poured into Type 1 (borosilicate glass) vials and the same volume was kept apart and stored at 3 °C for further analyses of each solution before starting the experiments to follow possible differences in the concentration of each factor; d) the selected pyrite crystals were immersed in their respective solution and each vial was purged with a gentle nitrogen steam to remove as much dissolved oxygen as possible.

To minimize the remaining dissolved oxygen in the system, a septum and two syringes as in-let out-let were used during the purge procedure. Vials were closed with a cap and extra parafilm protection was added to the exterior, minimizing cross-contamination in case of accidental dropping of vials. All vials were placed in the adequate recipient, which was rinsed with a silicon-based thermal fluid. The recipient was placed on a hotplate at constant temperature of 42 °C to mimic AMD conditions (Edwards and B.M.G., 1999). The system was let evolving for 60 days by periodically controlling the temperature to avoid overheating and gently manually shaking the vials, avoiding the use of stirring bars not to damage the crystals. In the rest of the text, day 0 samples will be referred to as t_0, whereas samples after 60 days of weathering will be referred to as t_f. "Sample" can refer to either a pyrite crystal or its solution in one of the 16 experiments performed, from N1 to N16.

2.6. ICP-OES analysis

Metal concentration in each solution was measured at t_0 and t_f. A proper calibration was made for each analyte by measuring the intensity of emission wavelength lines providing the maximum signal intensity and minimum spectral interferences for Na, K, Ca, Mg, Si, Sr, and Fe (589.592, 766.490, 393.366, 280.271, 251.611, 407.771 and 238.204 nm, respectively) covering the working linear concentration range of each analyte within the experimental domain. Samples were properly diluted in nitric acid (1 % *v*/v) and three replicates were measured. Results are shown in Table S3.

2.7. Ion chromatography analysis

Anion concentration in each solution was measured at t_0 and t_f by using an 8.0 mM Na_2CO_3 /1.0 mM $NaHCO_3$ mixture solution as eluent, at a flow of 0.5 mL min^{-1}. A calibration was made covering the working linear concentration range of each analyte. Separation was carried out for 20 min using an isocratic gradient and obtaining a good separation of the different analytes. The area of each peak was manually selected and used as an analytical parameter for quantification and three replicates for each sample were measured. For quantification of SO_4^{2-} additional dilutions were needed in some of the t_f samples. Results are shown in Table S4.

2.8. Raman mapping

To assess sulfur spatial distribution on the surface before extraction and to identify mineralogical phases, Raman maps were acquired on the surface of all studied pyrite crystals with a 15 μm spatial resolution in the X- and Y- directions and a grid of 40 × 40 points. The spectral range was 145 to 1912 cm^{-1} in all experiments with an average spectral resolution of 1.7 cm^{-1}. All Raman images acquired in the different experiments were assembled in an orderly fashion into a single image and analyzed at the same time under the assumption that single images are not representative of all the elemental sulfur produced on each sample, because only a small area of the surface of each crystal could be covered. The data were then organized into a three-dimensional dataset, the first two dimensions being associated with the spatial coordinates of each pixel in the image and the third dimension corresponding to the spectral information. Pixels with a very low signal-to-noise ratio, as well as cosmic peaks or saturated pixels were identified by outlier diagnostic based on Hotelling's T^2 and Q residuals (Bro and Smilde, 2014) and

omitted from the dataset. In total 2822 out of 25,600 pixels were left out. A baseline correction was applied to each pixel by adapting the spectral signal to an asymmetric truncated quadratic cost-function (Mazet et al., 2005) of order 8 and a threshold of 0.1. These parameters were previously tested and optimized to avoid fake Raman peaks or loss of spectral information near the limits of the spectral range. Then, Savitzky-Golay smoothing was applied to the Raman spectra with a polynomial degree of 2 and a 7 points windows and additive scattering effects were corrected by applying a Standard Normal Variate (SNV) (Fearn et al., 2009) to each Raman spectrum. All subsequent hyperspectral analyses followed the methodology described in (Muñoz et al., 2023) by using in-house MATLAB routines and HYPER-Tools 3.0 toolbox (Mobaraki and Amigo, 2018).

2.9. Elemental sulfur quantification

After the conclusion of weathering experiments, the vials were opened, and each crystal was separated from the solution, carefully cleaned with a laboratory paper tissue to avoid residues, accurately weighed again and stored in clean vials. The extraction procedure for elemental sulfur produced on the surface was as follows: 1) samples were immersed in carbon disulfide for 2 h; 2) pyrite crystals were removed from vials and a nitrogen steam was used until complete evaporation of carbon disulfide. All operations were carried out in a fume hood with extreme caution, avoiding the use of light bulbs because of the high volatility and flammability of carbon disulfide. During this operation, a crystallization of the remaining substance on the walls of the vial was observed; 3) 2.5 mL of perchloroethylene were added and left overnight with a magnetic stirring bar; 4) to obtain three experimental replicates for each pyrite sample, three 0.5 mL aliquots of this solution were placed into different vials and all the solvent was evaporated with nitrogen; 5) 0.5 mL of methanol were added to each vial before analysis.

For calibration, stock sulfur solutions in methanol were prepared ranging from 0.02 to 100 mg L^{-1}. Working in isocratic gradient for 5 min with a 95:5 MeOH/H_2O mobile phase and 1 mL min^{-1} flow, the sulfur peak at ~3.44 min was detected in the DAD by using the 254 nm wavelength, as shown in Fig. S1 for both standards and samples. In these chromatographic conditions, a good separation of elemental sulfur was achieved with no other co-eluted peaks. The area of the peaks was calculated and related to the sulfur concentration in solution based on the calibration line.

3. Results and discussion

3.1. Evaluation of the factors considered in pyrite weathering

The amount of elemental sulfur extracted and subsequently quantified for all the experiments is reported in Table 1, along with the mass loss for each pyrite crystal at the end of the experiment (reported as mass difference in absolute value). If AMD conditions are simulated, the highest amount of sulfur produced by oxidative weathering is obtained in experiments N1 and N12, whereas for experiments N2, N5, N7, N9, N10, N13, and N15, the amount of sulfur extracted is relatively low.

Linear regression was calculated by means of Partial Least Squares (PLS) to get coefficients and to establish the relationships between factors and the amount of elemental sulfur extracted from each crystal. The significance of one factor is measured with respect to its coefficient value: the higher a coefficient (in absolute value) the higher the significance. Two dummy factors, which can be associated to non-significant effects, were initially added to the design to check the significance of the calculated coefficients by comparing with that of dummy factors, as suggested in (Brereton, 2003).

Therefore, the model was calculated by using the real concentration values of the metallic and anionic factors measured at t_0 (Tables S3 and S4, respectively). If those values are compared with the experimental plan reported in Table S2, then minor deviations are noted. However, for the Si factor a significant error was introduced during either the preparation of the standard solutions or quantification. To maintain as much orthogonality as possible in the design, the Si factor was left out of the evaluation and replaced by a third dummy factor, so that the experimental matrix remains essentially the same. The resulting dataset thus included 16 samples at t_0 and 15 factors. The coefficients of the respective PLS regression model are reported in Fig. 1.

Table 1
Amount of elemental sulfur expressed in μg and reported as the mean value ± standard deviation of the mean. Mass loss, expressed in mg as the difference between the mass of pyrite crystal at t_f and t_0 in absolute value.

Sample	μg S^0	Δw(mg)
N1	305.4 ± 4.1	13.7
N2	7.7 ± 0.1	0.5
N3	114.6 ± 0.7	8.4
N4	124.8 ± 1.0	10.9
N5	6.6 ± 0.1	0.3
N6	52.1 ± 0.5	2.6
N7	6.6 ± 0.1	0.7
N8	56.0 ± 0.3	2.1
N9	8.2 ± 0.1	1.0
N10	4.7 ± 0.1	0.3
N11	17.3 ± 0.1	2.2
N12	278.4 ± 1.3	13.6
N13	5.9 ± 0.1	0.8
N14	68.4 ± 0.6	3.3
N15	4.7 ± 0.1	0.2
N16	10.9 ± 0.1	0.5

The largest coefficients are associated with Fe^{3+}, humic acid, and size factors, which can be considered important because they largely exceed the coefficients of the three dummy factors. Fe^{3+} concentration and crystal size have positive effects on the produced S, whereas humic acid has a negative effect, i.e., S decreases with increasing concentration of humic acid.

To better understand the evolution of each factor from t_0 to t_f, a dataset was built joining the metal and anionic concentrations given in Tables S3 and S4, and a principal component analysis (PCA) was carried out to furtherly evaluate changes that occurred during the simulated weathering. The dataset employed included all t_0 and t_f samples (32 in total) and 12 factors (Si factor was excluded). The scores and loadings

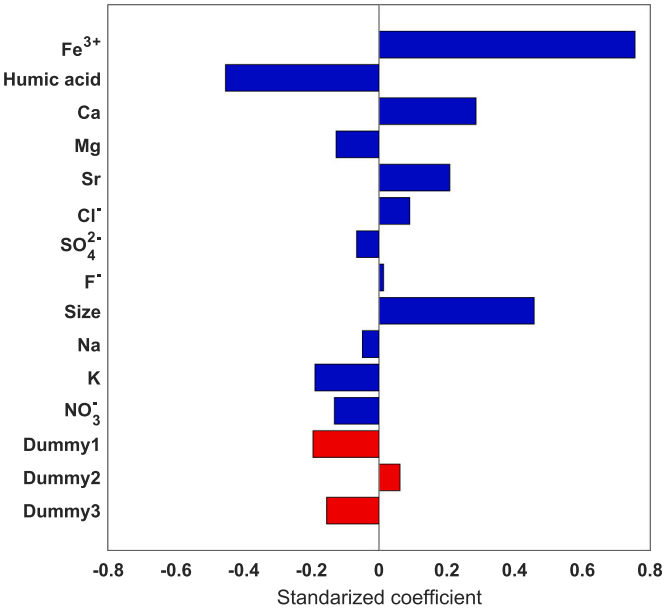

Fig. 1. Coefficients of the PLS models calculated with 6 latent variables (LVs) over elemental sulfur amount (expressed in logarithmic scale) response.

plot are reported in Fig. 2 (a) and (b), respectively. For a better interpretation of the results, in Fig. 2 (a) the samples have been colored according to whether they belong to t_0 or t_f. The first two principal components (PCs) explain approximately 56 % of data variance.

Fig. 2 (a) shows that t_0 samples are characterized by minor variability and better clustered than t_f samples, which is ascribed to relevant changes during the experiments. As shown in the score and loading plots, PC2 mainly explains the difference between N1 and N12 samples at t_f (mainly characterized by high levels in the Fe and SO_4^{2-} factors) and the rest of the samples (especially t_0 samples). In contrast, PC1 highlights the differences between N5 sample at t_f (negative scores) and other samples, which indicates a greater net increase of the Na, K, Ca and Sr factors.

Subsequently, correlation values were calculated between the amount of sulfur extracted and the difference of total iron ($Fe^{2+} + Fe^{3+}$) and SO_4^{2-} factors (e.g. $\Delta[Fe] = [Fe]_{tf} - [Fe]_{t0}$), as shown in Fig. S2 (a) and (b). According to the correlation between the change on the total iron and sulfur concentration and the amount of elemental sulfur extracted (0.9913 and 0.9872, respectively), it can be concluded that the greater the total concentration of Fe and SO_4^{2-} in solution at t_f, the greater the elemental sulfur produced with a linear positive correlation. Similar plots are reported in Fig. S2 (c) and (d) but considering net mass (reported in Table 1) instead of elemental sulfur as response. The correlation values with respect to total iron (0.980) and sulfate differences (0.948), demonstrate these factors are also correlated with mass loss response, indirectly suggesting a linear positive correlation between elemental sulfur and mass loss responses, as shown in Fig. S3, with a correlation value of 0.956.

Finally, a new dataset including 16 samples and 12 factors was created using the difference of each factor between t_f and t_0 as values. A further PCA model was calculated and the corresponding scores and loadings plots are reported in Fig. S4 (a) and (b) by coloring the samples with respect to the elemental sulfur response. The first two PCs explain ~62 % of total variance. There is a trend regarding the amount of sulfur from samples with positive and negative scores for PC1 and PC2, respectively, to samples with negative and positive scores for PC1 and PC2, respectively. Samples N1 and N12, those with the highest amount of sulfur, are characterized by a net increment with respect to the total amount of Fe, SO_4^{2-} and F^- in solution. As done for the first PLS model, three dummy factors were included in this new dataset (16 samples and 15 factors) which was used to calculate a second PLS regression model (coefficients reported in Fig. S5). Concentration differences of total Fe, Cl^-, F^- and SO_4^{2-}, already highlighted by previous PCA analysis, appeared to be significant factors (i.e., coefficients larger than those associated to dummy factors). The apparent importance of Cl^- could be explained in terms of the experimental error of the measurements because the net difference for this factor is zero in most cases. The significance of F^- requires a more detailed explanation. A depletion of F^- in solution, as found for instance in samples N2, N5 and N7, seems to be associated with low amounts of elemental sulfur, whereas for samples N1 and N12 the concentration difference is high and positive, despite the negative coefficient of this factor. This leads us to think of a possible interaction effect of this factor with another one, not contemplated in the actual Plackett-Burman design. A mechanistic interpretation of the results regarding the fate of F^- and the demonstration of a likely indirect influence in the weathering of pyrite in acidic waters requires additional studies on the speciation of F, which is beyond the scope of the present study.

In conclusion, a high initial concentration of ferric iron (t_0) leads to the generation of remarkable amounts of elemental sulfur in fresh pyrite crystals (being the concentration of SO_4^{2-} at t_0 not significant). However, the higher the concentration of SO_4^{2-} and total iron in solution at t_f, the greater the amount of sulfur expected on the surface of oxidized pyrite crystals.

3.2. Chemical discussion on the effect of significant factors for OWP

Although the elemental reactions that comprise the oxidative weathering of pyrite would be on the order of hundreds, some assumptions can be made based on the significance of ferric iron factor, without taking into account surficial, electrochemical or photochemical considerations that are beyond the scope of this study. Nevertheless, it is widely accepted that ferric iron as oxidant and thiosulfate as an initial soluble intermediate are central concerning pyrite oxidation pathways. When considering circumneutral pH waters, relatively high amounts of thiosulfate and polythionates are reported (Moses et al., 1987; Schippers et al., 1996, 1999). However, a rapid conversion of thiosulfate to tetrathionate, which further oxidizes into sulfate, is observed in acidic waters produced in many acid mine drainage locations (Rimstidt and Vaughan, 2003; Descostes et al., 2004). When there is an excess of ferric

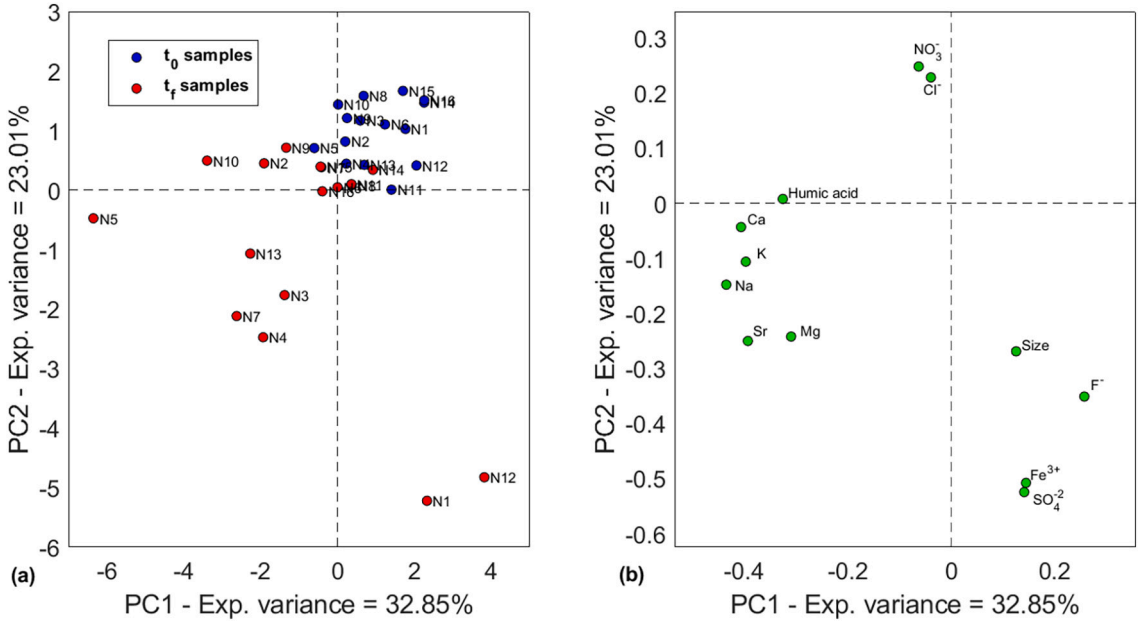

Fig. 2. Scores (a) and loadings (b) plot using the real values of the factors as dataset, before and after the conclusion of the experiments.

iron, at pH =1.5 the conversion of thiosulfate to tetrathionate is almost complete (Druschel et al., 2003a). On the contrary, when ferric iron is depleted, some elemental sulfur formation is expected, even if polythionates are the predominant products. Elemental sulfur could be formed from thiosulphate disproportionation (Heunisch, 1977; Williamson and Rimstidt, 1993; L. III, 1997), which reaction shown in (5) is a reversible equilibrium, being completely displaced to the right when pH is below 2.

$$8\,S_2O_3^{2-} + 8H^+ \rightleftharpoons S_{8(s)} + 8\,HSO_3^- \quad (5)$$

$$2S_2O_3^{2-} + 2Fe^{3+} \rightarrow Fe\left(S_2O_3^{2-}\right)^+ \quad (6)$$

$$Fe\left(S_2O_3^{2-}\right)^+ \rightarrow S_4O_6^{2-} + 2Fe^{2+} \quad (7)$$

Thiosulfate disproportionation is in competition with thiosulfate reaction with ferric iron (6) and (7), so reaction (5) is only expected when ferric iron is depleted. This is explained if, below pH 1.7, ferric oxidation forms tetrathionate (eventually decomposing into sulfate) slightly faster than thiosulphate disproportionation (Williamson and Rimstidt, 1993). The kinetics of (6) will depend on the starting concentration of ferric iron and thiosulfate in solution to form the Fe $(S_2O_3^{2-})^+$ complex. Both HSO_3^- and $S_4O_6^{2-}$ react further to form SO_4^{2-} in acidic conditions, which could explain the considerable net increase found after two months of oxidation experiments. Other studies suggest different pathways for elemental sulfur formation from that of thiosulfate (Biegler and Swift, 1979; Flatt and Woods, 1995; Holmes and Crundwell, 2000), involving polysulfide intermediates at an S-enriched pyrite surface, as stated in the inhibition of S polymerization by Fe study (Harmer and Nesbitt, 2004).

Because all crystals used in the experiments have similar morphology, a plausible explanation of the importance of the size factor is that the larger the surface area available for oxidation, the greater the amount of sulfur produced, because more reactive sites are available for thiosulfate formation. Crystalline defects may play an important role in pyrite oxidation and they must be considered as well, as electron deficiency sites at the surface may lead to different oxidation pathways involving interaction with water molecules and hydroxyl radicals (Borda et al., 2001, 2003, Druschel et al., 2003b).

Specific characterization studies should be conducted to analyze the interaction between humic acid molecules and pyrite surface to explain the negative influence of humic acids in AMD conditions with respect to the release of thiosulfate into solution and the consequent formation of elemental sulfur on the surface of the crystal. In (Zheng et al., 2019), the interaction of humic acids with the surface of pyrite was explained by electrochemical reactions: humic acids adsorbed on the pyrite surface inhibit the further transformation of sulfur without affecting the weathering mechanism.

3.3. Raman hyperspectral image analysis

To confirm whether the weathering experiments led to pyrite oxidation, a comparison was made between Raman images of a recognizable area of a randomly selected sample (N12) before and after the weathering simulation at the laboratory scale, that is, at t_0 and t_f. For this scope, several fresh pyrite crystals from the same locality were previously analyzed and their average spectrum was then calculated, which included the three main vibrational modes of pyrite. Afterwards, this spectrum was used as a reference to calculate a Pearson correlation model for the same area of N12 at t_0 and t_f. As seen in Fig. 3 (c), the surface of N12 sample at t_0 shows no other vibrational modes than those typically associated with pyrite (343, 379 and 431 cm^{-1} wavenumbers), depicted from the large number of pixels colored in green, corresponding to a correlation value close to 1. After 60 days of oxidation, spectral differences are noticeable for most of the pixels, confirming that major chemical changes occurred on the surface of the pyrite crystal, as shown in Fig. 3 (b) and (d).

For the rest of the samples, Raman images were acquired before extraction of elemental sulfur and analyzed to determine the spatial distribution of the sulfur formed on the surface of the pyrite crystals and check for additional weathering products, if any.

First, a PCA analysis was carried out and the score maps and loading plots for the first three principal components, which explain ~78 % of data variance, are shown in Fig. 4. PC1 highlights the difference between pixels showing positive scores characterized by 151, 218 and 471

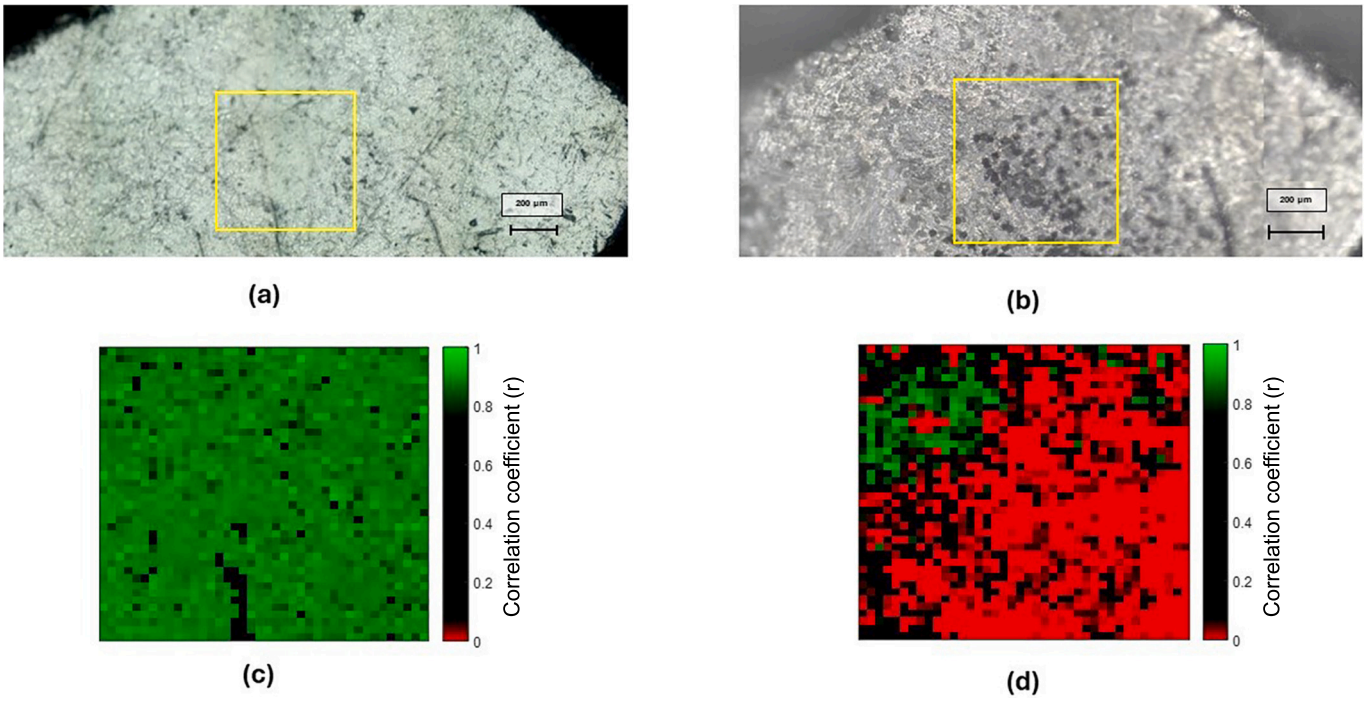

Fig. 3. Real images of sample N12 at t_0 (a) and t_f (b). Pearson correlation model by using a pyrite reference spectrum at t_0 (c) and t_f (d).

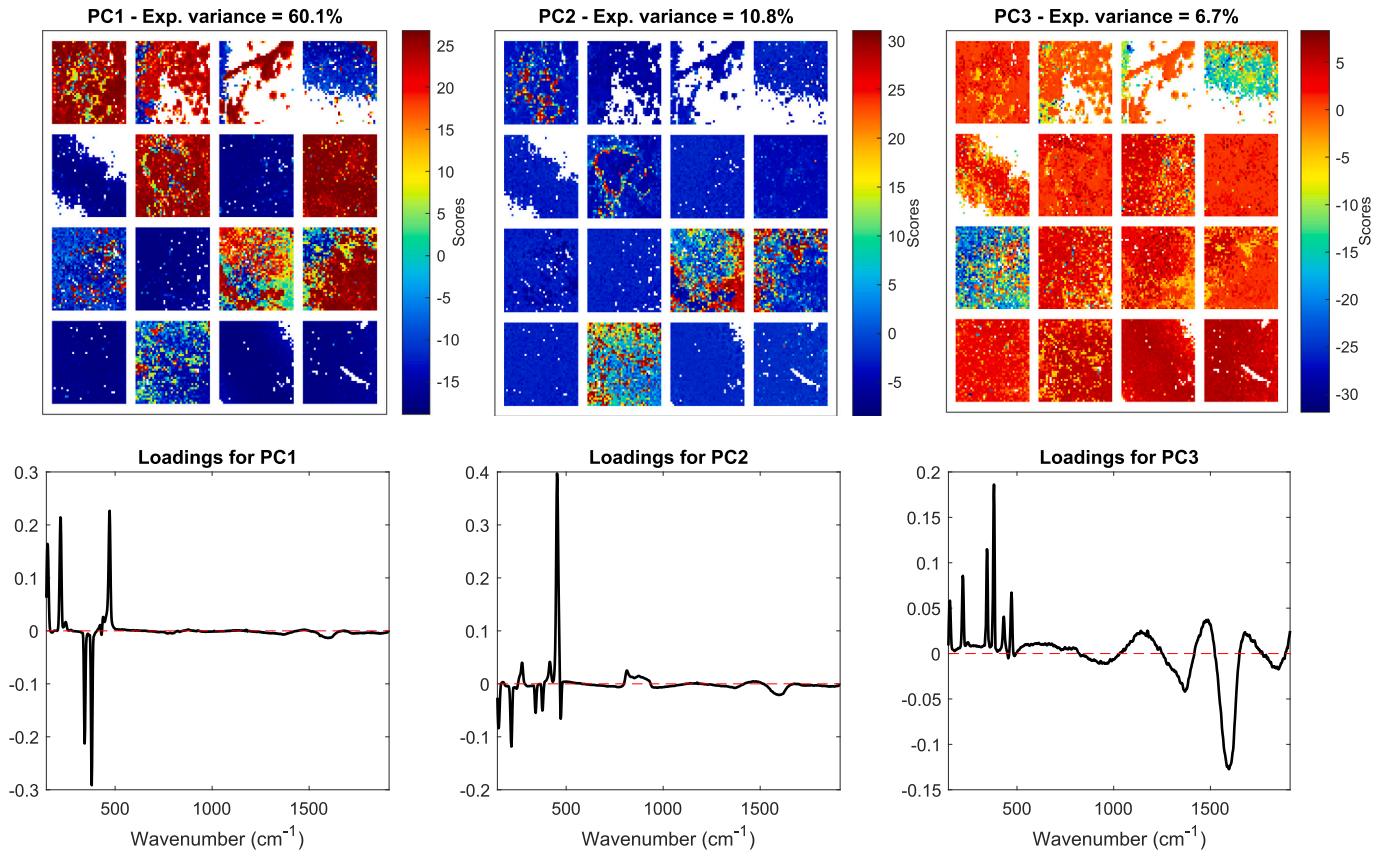

Fig. 4. PCA score maps (upper) and loadings (bottom). From left to right and from up to down, samples N1 to N16.

cm^{-1} wavenumbers, which are characteristic vibrational modes of elemental sulfur, and the rest of the pixels with negative scores, mainly characterized by 343 and 379 cm^{-1} wavenumbers, two of the main vibrational modes of pyrite. On the other hand, PC2 mainly explains variance related to pixels with positive scores for which 272, 415 and especially, 453 cm^{-1} wavenumbers are important. Finally, unclear separation between pixels is depicted from scores map of PC3, except for pixels with very high positive scores, for which a combination of the same wavenumbers with positive and negative loadings already seen in the PC1 seems to be important. In addition, two broad bands in the 1300–1700 cm^{-1} region, typically associated with low-crystalline mineralogical phases, may be associated with pixels of negative scores.

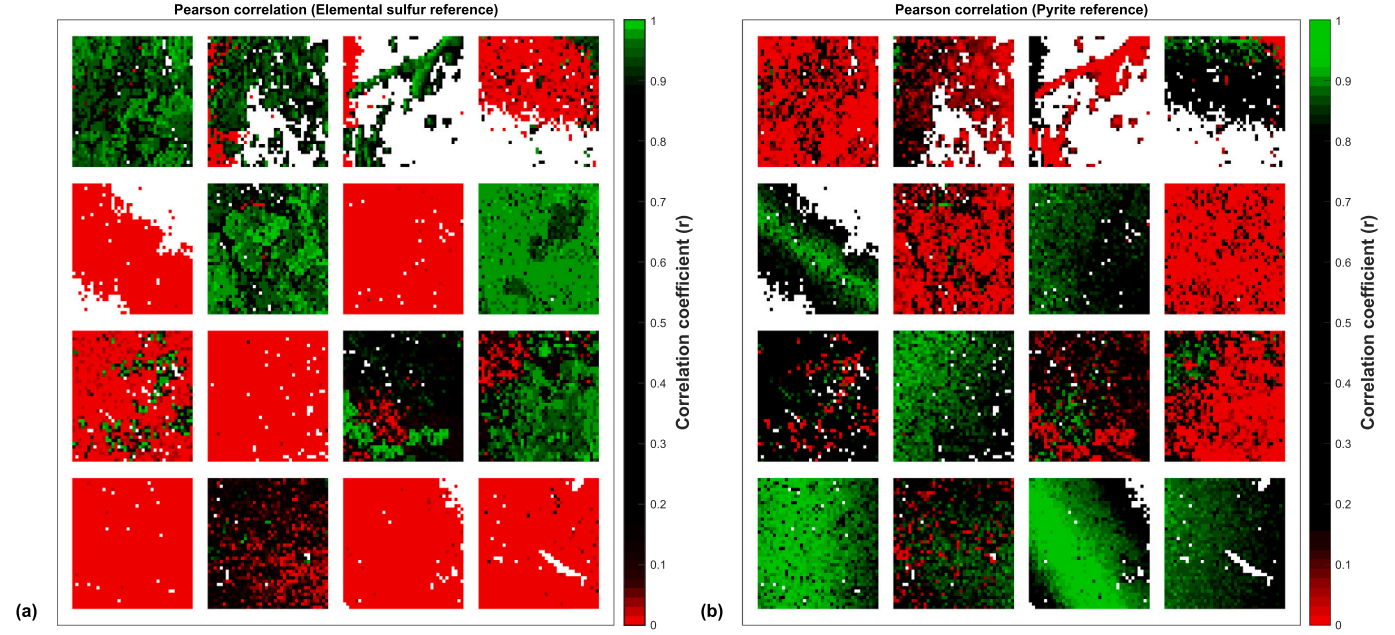

Fig. 5. Pearson correlation calculated using an elemental sulfur (a) and pyrite (b) reference spectrum. From left to right and from up to down, samples N1 to N16.

To better assess the spatial distribution of elemental sulfur on the surface, Pearson correlations were calculated using as reference: a) an elemental sulfur spectrum acquired from a high-purity standard powder; b) the average spectrum of the fresh surface of pyrite crystal from Val Trebbia, as previously done for N12. A visual representation of the spatial distribution of elemental sulfur and pyrite, colored according to the respective calculated pixel correlation values, is shown in Fig. 5 (a) and (b). As seen in Fig. 5 (a), sulfur is homogeneously distributed across the surface, contrary to what concluded in (McGuire et al., 2001). The identified sulfur in the analyzed images does not necessarily correspond to those samples with the highest amount of elemental sulfur extracted, because only a small fraction of the surface was analyzed with Raman. Despite the small area covered, sulfur forms patches of considerable size ($>600\ \mu m^2$ for samples N1, N6, and N8) and thickness, because no pyrite vibrational modes are revealed in the spectra associated with those pixels. Finally, Fig. 5 (b), highlights areas of pixels with correlations between 0.1 and 0.9 (black pixels), for which spectral information may result from a combination of vibrational modes from different mineralogical phases such as pyrite and sulfur.

4. Conclusion

The proposed experiments at laboratory scale for the assessment of oxidative weathering of pyrite in acid solution prove to be a valuable methodology for the screening of different factors and could be extended to the study of pyrite weathering under conditions other than acid mine drainage on shorter time scales than in nature. For this scope, Design of experiments methodology was employed to determine the main factors that characterized OWP in the studied conditions. Once the significant factors are identified and the effect of those factors over a response is clearly understood, a second optimization stage can be performed for the minimization or maximization of a certain response. This could help minimize the sulfuric acid production derived from OWP and therefore, the acidification of natural environments.

The determined different quantities of elemental sulfur among samples, supported by Raman spectroscopy results, confirm that the concentration of ferric iron is the rate limiting step for the OWP at low pH waters rather than dissolved oxygen. The presence of sulfur, which is homogeneously distributed on the surface of pyrite, is a symptom of ferric iron depletion, because thiosulphate preferentially reacts with ferric iron to form tetrathionate, which eventually decomposes into sulfate, rather than disproportionate into sulfur and hydrogen sulfite. A fuller understanding of oxidative weathering of pyrite necessitates further experimental studies that consider the influence of dissolved oxygen, as well as thiosulfate, and polythionates or even bacterial action. Morphology must also be considered as a factor for a better understanding of the reactions that take place on the surface of the pyrite crystals.

CRediT authorship contribution statement

Enmanuel Cruz Muñoz: Writing – original draft, Software, Methodology, Investigation, Formal analysis, Data curation, Conceptualization. **Fabio Gosetti:** Writing – review & editing, Writing – original draft, Supervision, Resources, Project administration, Methodology, Investigation, Conceptualization. **Sergio Andò:** Writing – review & editing, Supervision, Resources, Formal analysis. **Davide Ballabio:** Writing – review & editing, Validation, Supervision, Software, Methodology, Investigation, Formal analysis, Conceptualization. **Eduardo Garzanti:** Writing – review & editing, Supervision, Resources.

Declaration of competing interest

The authors declare the following financial interests/personal relationships which may be considered as potential competing interests: Fabio Gosetti reports financial support was provided by Italian Ministry of Education, University and Research (MIUR). Enmanuel Cruz reports financial support was provided by Italian Ministry of Education, University and Research (MIUR). If there are other authors, they declare that they have no known competing financial interests or personal relationships that could have appeared to influence the work reported in this paper.

Data availability

Data will be made available on request.

Acknowledgements

The research is funded by the Italian MIUR project Dipartimenti di Eccellenza 2018-2022.

Appendix A. Supplementary data

Supplementary data to this article can be found online at https://doi.org/10.1016/j.scitotenv.2024.176284.

References

Amrish, V.N., Arun, K., Nishitha, D., Balakrishna, K., Udayashankar, H.N., Khare, N., 2022. Major ion chemistry and silicate weathering rate of a small Western Ghats river, Sharavati, southwestern India. Appl. Geochem. 136, 105182.
Berner, R.A., 1987. Models for carbon and sulfur cycles and atmospheric oxygen: application to Paleozoic geologic history. Am. J. Sci. 287 (3), 177–196.
Berner, R.A., 2009. Phanerozoic atmospheric oxygen: new results using the geocarbsulf model. Am. J. Sci. 309 (7), 603–606.
Biegler, T., Swift, D.A., 1979. Anodic behaviour of pyrite in acid solutions. Electrochim. Acta 24 (4), 415–420.
Borda, M.J., Elsetinow, A.R., Schoonen, M.A., Strongin, D.R., 2001. Pyrite-induced hydrogen peroxide formation as a driving force in the evolution of photosynthetic organisms on an early earth. Astrobiology 1 (3), 283–288.
Borda, M.J., Elsetinow, A.R., Strongin, D.R., Schoonen, M.A., 2003. A mechanism for the production of hydroxyl radical at surface defect sites on pyrite. Geochim. Cosmochim. Acta 67 (5), 935–939.
Brereton, R.G., 2003. Chemometrics. Wiley.
Bro, R., Smilde, A.K., 2014. Principal component analysis. Anal. Methods 6 (9), 2812–2831.
Brown, A.D., Jurinak, J.J., 1989. Mechanism of pyrite oxidation in aqueous mixtures. J. Environ. Qual. 18 (4), 545–550.
Buckley, A.N., Woods, R., 1987. The surface oxidation of pyrite. Appl. Surf. Sci. 27 (4), 437–452.
Bufe, A., Hovius, N., Emberson, R., Rugenstein, J.K.C., Galy, A., Hassenruck-Gudipati, H. J., Chang, J.M., 2021. Co-variation of silicate, carbonate and sulfide weathering drives CO2 release with erosion. Nat. Geosci. 14 (4), 211–216.
Calmels, D., Gaillardet, J., Brenot, A., France-Lanord, C., 2007. Sustained sulfide oxidation by physical erosion processes in the Mackenzie River basin: climatic perspectives. Geology 35 (11), 1003–1006.
Cartwright, I., 2020. Concentration vs. streamflow (C-Q) relationships of major ions in south-eastern Australian rivers: sources and fluxes of inorganic ions and nutrients. Appl. Geochem. 120, 104680.
Chandra, A.P., Gerson, A.R., 2010. The mechanisms of pyrite oxidation and leaching: a fundamental perspective. Surf. Sci. Rep. 65 (9), 293–315.
de Donato, P., Mustin, C., Benoit, R., Erre, R., 1993. Spatial distribution of iron and Sulphur species on the surface of pyrite. Appl. Surf. Sci. 68 (1), 81–93.
Demoisson, F., Mullet, M., Humbert, B., 2007. Investigation of pyrite oxidation by hexavalent chromium: solution species and surface chemistry. J. Colloid Interface Sci. 316 (2), 531–540.
Descostes, M., Vitorge, P., Beaucaire, C., 2004. Pyrite dissolution in acidic media. Geochim. Cosmochim. Acta 68 (22), 4559–4569.
Druschel, G.K., Hamers, R.J., Banfield, J.F., 2003a. Kinetics and mechanism of polythionate oxidation to sulfate at low pH by O2 and Fe3+. Geochim. Cosmochim. Acta 67 (23), 4457–4469.
Druschel, G.K., Hamers, R.J., Luther III, G.W., Banfield, J.F., 2003b. Kinetics and mechanism of Trithionate and Tetrathionate oxidation at low pH by hydroxyl radicals. Aquat. Geochem. 9 (2), 145–164.
Edwards, Katrina J., B.M.G., 1999. Geomicrobiology of pyrite (FeS2) dissolution: case study at Iron Mountain. California. Geomicrobiol J. 16 (2), 155–179.
Elsetinow, A.R., Borda, M.J., Schoonen, M.A.A., Strongin, D.R., 2003. Suppression of pyrite oxidation in acidic aqueous environments using lipids having two hydrophobic tails. Adv. Environ. Res. 7 (4), 969–974.
Evangelou, V.P. (Bill), Zhang, Y.L., 1995. A review: pyrite oxidation mechanisms and acid mine drainage prevention. Crit. Rev. Environ. Sci. Technol. 25 (2), 141–199.
Fearn, T., Riccioli, C., Garrido-Varo, A., Guerrero-Ginel, J.E., 2009. On the geometry of SNV and MSC. Chemom. Intell. Lab. Syst. 96 (1), 22–26.

Flatt, J.R., Woods, R., 1995. A voltammetric investigation of the oxidation of pyrite in nitric acid solutions: relation to treatment of refractory gold ores. J. Appl. Electrochem. 25 (9).
Fowler, T., Holmes, P., Crundwell, F., 2001. On the kinetics and mechanism of the dissolution of pyrite in the presence of Thiobacillus ferrooxidans. Hydrometallurgy 59 (2–3), 257–270.
G., B., 2008. I minerali del piacentino – come riconoscerli dove trovarli. Tipolito Farnese, Piacenza.
Giannetti, B.F., Bonilla, S.H., Zinola, C.F., Rabóczkay, T., 2001. Study of the main oxidation products of natural pyrite by voltammetric and photoelectrochemical responses. Hydrometallurgy 60 (1), 41–53.
Harmer, S.L., Nesbitt, H.W., 2004. Stabilization of pyrite (FeS2), marcasite (FeS2), arsenopyrite (FeAsS) and loellingite (FeAs2) surfaces by polymerization and auto-redox reactions. Surf. Sci. 564 (1–3), 38–52.
Heunisch, G.W., 1977. Stoichiometry of the reaction of sulfites with hydrogen sulfide ion. Inorg. Chem. 16 (6), 1411–1413.
Holmes, P.R., Crundwell, F.K., 2000. The kinetics of the oxidation of pyrite by ferric ions and dissolved oxygen: an electrochemical study. Geochim. Cosmochim. Acta 64 (2), 263–274.
Jameson, R., 2011. Manual of Mineralogy. Wiley, Manual of mineralogy.
Jervis, G., 1874. I tesori sotterranei dell'Italia. In: Regione dell'Appennino e vulcani attivi e spenti, vol. 2. Loescher, Torino.
Keith, C.N., Vaughan, D.J., 2000. Mechanisms and rates of sulphide oxidation in relation to the problems of acid rock (mine) drainage. In: Environmental Mineralogy<subtitle>Microbial Interactions, Anthropogenic Influences, Contaminated Land and Waste Management</subtitle>. Mineralogical Society of Great Britain and Ireland.
Kelsall, G.H., Yin, Q., Vaughan, D.J., England, K.E.R., Brandon, N.P., 1999. Electrochemical oxidation of pyrite (FeS2) in aqueous electrolytes. J. Electroanal. Chem. 471 (2), 116–125.
Kemeny, P.C., Lopez, G.I., Dalleska, N.F., Torres, M., Burke, A., Bhatt, M.P., West, A.J., Hartmann, J., Adkins, J.F., 2021. Sulfate sulfur isotopes and major ion chemistry reveal that pyrite oxidation counteracts CO2 drawdown from silicate weathering in the Langtang-Trisuli-Narayani River system, Nepal Himalaya. Geochim. Cosmochim. Acta 294, 43–69.
L. III, G.W., 1997. Comment by G. W. Luther III on "Confirmation of a sulfur-rich layer on pyrite after oxidative dissolution by Fe(III) ions around pH 2". Geochim. Cosmochim. Acta 61 (15), 3273–3274.
Madhavan, N., Subramanian, V., 2001. Fluoride concentration in river waters of South Asia. Curr. Sci. 80 (10), 1312–1319.
Margitan, J.J., 1984. Mechanism of the atmospheric oxidation of sulfur dioxide. Catalysis by hydroxyl radicals. J. Phys. Chem. 88 (15), 3314–3318.
Mazet, V., Carteret, C., Brie, D., Idier, J., Humbert, B., 2005. Background removal from spectra by designing and minimising a non-quadratic cost function. Chemom. Intell. Lab. Syst. 76 (2), 121–133.
McGuire, M.M., Jallad, K.N., Ben-Amotz, D., Hamers, R.J., 2001. Chemical mapping of elemental sulfur on pyrite and arsenopyrite surfaces using near-infrared Raman imaging microscopy. Appl. Surf. Sci. 178 (1–4), 105–115.
McKibben, M.A., Barnes, H.L., 1986a. Oxidation of pyrite in low temperature acidic solutions: rate laws and surface textures. Geochim. Cosmochim. Acta 50 (7), 1509–1520.
McKibben, M.A., Barnes, H.L., 1986b. Oxidation of pyrite in low temperature acidic solutions: rate laws and surface textures. Geochim. Cosmochim. Acta 50 (7), 1509–1520.
Mobaraki, N., Amigo, J.M., 2018. HYPER-tools. A graphical user-friendly interface for hyperspectral image analysis. Chemom. Intell. Lab. Syst. 172, 174–187.
Moses, C.O., Herman, J.S., 1991. Pyrite oxidation at circumneutral pH. Geochim. Cosmochim. Acta 55 (2), 471–482.
Moses, C.O., Kirk Nordstrom, D., Herman, J.S., Mills, A.L., 1987. Aqueous pyrite oxidation by dissolved oxygen and by ferric iron. Geochim. Cosmochim. Acta 51 (6), 1561–1571.
Muñoz, E.C., Gosetti, F., Ballabio, D., Andò, S., Gómez-Laserna, O., Amigo, J.M., Garzanti, E., 2023. Characterization of pyrite weathering products by Raman hyperspectral imaging and chemometrics techniques. Microchem. J. 190 (February).
Rickard, D., Mussmann, M., Steadman, J.A., 2017. Sedimentary sulfides. Elements 13 (2), 117–122.
Rimstidt, J.D., Vaughan, D.J., 2003. Pyrite oxidation: a state-of-the-art assessment of the reaction mechanism. Geochim. Cosmochim. Acta 67 (5), 873–880.
Samanta, A., Tripathy, G.R., Das, R., 2019. Temporal variations in water chemistry of the (lower) Brahmaputra River: implications to seasonality in mineral weathering. Geochem. Geophys. Geosyst. 20 (6), 2769–2785.
Sasaki, K., Tsunekawa, M., Ohtsuka, T., Konno, H., 1997. Reply to the comment by G. W. Luther III on "confirmation of a sulfur-rich layer on pyrite after oxidative dissolution by Fe(III) ions around pH 2". Geochim. Cosmochim. Acta 61 (15), 3273–3274.
Schaufuß, A.G., Nesbitt, H.W., Kartio, I., Laajalehto, K., Bancroft, G.M., Szargan, R., 1998. Incipient oxidation of fractured pyrite surfaces in air. J. Electron Spectrosc. Relat. Phenom. 96 (1–3), 69–82.
Schippers, A., Jozsa, P., Sand, W., 1996. Sulfur chemistry in bacterial leaching of pyrite. Appl. Environ. Microbiol. 62 (9), 3424–3431.
Schippers, A., Rohwerder, T., Sand, W., 1999. Intermediary sulfur compounds in pyrite oxidation: implications for bioleaching and biodepyritization of coal. Appl. Microbiol. Biotechnol. 52 (1), 104–110.
Singer, P.C., Stumm, W., 1970. Acidic mine drainage: the rate-determining step. Science 167 (3921), 1121–1123.
Todd, E.C., Sherman, D.M., Purton, J.A., 2003. Surface oxidation of pyrite under ambient atmospheric and aqueous (pH = 2 to 10) conditions: electronic structure and mineralogy from X-ray absorption spectroscopy. Geochim. Cosmochim. Acta 67 (5), 881–893.
Torres, M.A., West, A.J., Li, G., 2014. Sulphide oxidation and carbonate dissolution as a source of CO2 over geological timescales. Nature 507 (7492), 346–349.
Torrijos, R.C., Phan-Tan-Luu, R., 2020. Screening Strategies. *Comprehensive Chemometrics*. Elsevier, In, pp. 209–250.
Tsering, T., Abdel Wahed, M.S.M., Iftekhar, S., Sillanpää, M., 2019. Major ion chemistry of the Teesta River in Sikkim Himalaya, India: chemical weathering and assessment of water quality. J. Hydrol.: Reg. Stud. 24, 100612.
Vaughan, D.J., Corkhill, C.L., 2017. Mineralogy of sulfides. Elements 13 (2), 81–87.
Wenk, H.-R., Bulakh, A., 2004. Minerals: their constitution and origin, 42. Cambridge University Press, 388-405, 511-531.
Williamson, M.A., Rimstidt, J.D., 1993. The rate of decomposition of the ferric-thiosulfate complex in acidic aqueous solutions. Geochim. Cosmochim. Acta 57 (15), 3555–3561.
Yang, Y., Tan, S.N., Glenn, A.M., Harmer, S., Bhargava, S., Chen, M., 2015. A direct observation of bacterial coverage and biofilm formation by Acidithiobacillus ferrooxidans on chalcopyrite and pyrite surfaces. Biofouling 31 (7), 575–586.
Yu, J.-Y., McGenity, T.J., Coleman, M.L., 2001. Solution chemistry during the lag phase and exponential phase of pyrite oxidation by Thiobacillus ferrooxidans. Chem. Geol. 175 (3–4), 307–317.
Zhang, Z., Zhang, C., Yang, Y., Zhang, Z., Tang, Y., Su, P., Lin, Z., 2022. A review of sulfate-reducing bacteria: metabolism, influencing factors and application in wastewater treatment. J. Clean. Prod. 376 (May), 134109.
Zheng, K., Li, H., Xu, L., Li, S., Wang, L., Wen, X., Liu, Q., 2019. The influence of humic acids on the weathering of pyrite: electrochemical mechanism and environmental implications. Environ. Pollut. 251, 738–745.
Zhu, W., Reinfelder, J.R., 2012. The microbial community of a black shale pyrite biofilm and its implications for pyrite weathering. Geomicrobiol J. 29 (2), 186–193.